International Journal of Hydrogen Energy 263 (2026) 156682

Contents lists available at ScienceDirect

International Journal of Hydrogen Energy

journal homepage: www.elsevier.com/locate/he

Mechanochemically synthesized Cu-based TiO_2–$LaFeO_3$ ternary photocatalysts for efficient hydrogen generation under UV–visible light

Marica Muscetta [a,*], Isabella Natali Sora [b], Renato Pelosato [b], Adetunji Alabi [c,d], Israa Othman [e], Mohammad Abu Haija [e,f], Giovanni Palmisano [c,d], Roberto Andreozzi [a], Laura Clarizia [a,**]

[a] Department of Chemical, Materials and Production Engineering (DICMaPI), University of Naples Federico II, Piazzale V. Tecchio 80, Naples, 80125, Italy
[b] Department of Engineering and Applied Sciences, University of Bergamo, Viale Marconi 5, Dalmine, BG, 24044, Italy
[c] Department of Chemical and Petroleum Engineering, Khalifa University of Science and Technology, PO Box, Abu Dhabi, 127788, United Arab Emirates
[d] Research and Innovation Center on CO2 and H2 (RICH), Khalifa University of Science and Technology, P.O. Box 127788, Abu Dhabi, United Arab Emirates
[e] Department of Chemistry, Khalifa University of Science and Technology, PO Box 127788, Abu Dhabi, United Arab Emirates
[f] Center for Catalysis and Separation (CeCaS), Khalifa University of Science and Technology, P.O. Box 127788, Abu Dhabi, United Arab Emirates

A B S T R A C T

This study reports the development of novel Cu-based $LaFeO_3/TiO_2$ photocatalysts for sustainable hydrogen production via photocatalytic reforming of organic substrates under UV and visible light. Catalysts were synthesized using a simple powder-mixing method followed by ball milling, a straightforward and potentially scalable preparation approach. Initial screening studies of binary systems comprising TiO_2, CuO, Cu_2O, and $LaFeO_3$ identified 10 wt% CuO/TiO_2 and 3.86 wt% $LaFeO_3/TiO_2$ as the most active catalysts, achieving H_2 yields of 530 μmol and 486 μmol, respectively, after 3 h of irradiation. Guided by these results, ternary composites were designed by tuning component ratios while maintaining a total catalyst concentration of 0.2 g L^{-1}. The optimized CuO-based ternary catalyst (86.14 wt% TiO_2, 10 wt% CuO, 3.86 wt% $LaFeO_3$) delivered the highest H_2 evolution of 828 μmol after 3 h of irradiation under UV + visible irradiation, showing a substantial improvement compared with the corresponding binary systems. Cu_2O-based ternary materials exhibited improved stability after ball milling, with H_2 production increasing from 338 μmol to 440 μmol. Among sacrificial agents, glycerol proved most effective, followed by glucose and methanol. These findings demonstrate that $Cu_2O/LaFeO_3/TiO_2$ ternary photocatalysts are highly efficient, scalable, and robust materials for hydrogen generation, offering insights into synergistic interactions, structure-performance relationships, and catalyst optimization. The optimization of the experimental parameters (C_{cat} = 0.8 g L^{-1}, [Glycerol] = 0.05 M, T = 90°C) resulted in more than a 20-fold increase in H_2 production. By bridging fundamental photocatalysis with applied process design, this work contributes to the development of sustainable hydrogen production strategies, highlighting a practical pathway to advance renewable energy technologies and address the global energy transition.

1. Introduction

Within the framework of the ongoing energy transition, photocatalytic hydrogen generation has emerged as a promising alternative to conventional fossil fuel–based energy systems [1]. The continued use of fossil fuels does not only reduce their depletion, but also contributes to severe environmental challenges, such as greenhouse gas emissions, air pollution, and climate change. Photocatalytic processes provide a sustainable solution by harnessing solar energy, an abundant and renewable resource, to drive H_2 evolution [2]. The combination of photocatalysis with wastewater treatment introduces an added environmental benefit, due to the possibility of using organic compounds in wastewater as sacrificial agents, simultaneously allowing hydrogen generation and water remediation [3]. In this context, TiO_2 remains one of the most widely investigated photocatalysts due to its low cost, abundance, non-toxicity, and excellent thermal and chemical stability. These features have established it as a benchmark material in photocatalysis research. However, TiO_2 possesses a wide band gap (3.0–3.2 eV), which restricts its photoresponse to the UV region, thereby limiting its efficiency under natural sunlight where UV photons represent less than 5% of the spectrum. This limitation has stimulated extensive research into strategies to enhance its photocatalytic performance and extend its optical absorption into the visible range. Several modification approaches have been employed to overcome the drawbacks of pristine TiO_2. These include: i) the photodeposition of noble metals such as Au and Pt, which can serve as electron traps and promote

* Corresponding author.
** Corresponding author.
E-mail addresses: marica.muscetta@unina.it (M. Muscetta), laura.clarizia2@unina.it (L. Clarizia).

https://doi.org/10.1016/j.ijhydene.2026.156682
Received 20 December 2025; Received in revised form 7 July 2026; Accepted 16 July 2026
Available online 3 August 2026

charge separation [4], ii) the formation of heterojunctions with other semiconductors, such as oxides or chalcogenides, to facilitate interfacial charge transfer [5,6] and iii) the structural engineering of TiO_2 to tailor its morphology, defect concentration, or crystallinity [7]. Among these, the construction of heterojunctions has proven to be particularly effective, as coupling TiO_2 with suitable semiconductors can simultaneously enhance charge separation and broaden the absorption window into the visible-light range [8].

Recent studies have especially focused on the incorporation of copper-based species into TiO_2 matrices [9,10]. Copper, depending on its oxidation state and incorporation mechanism, can either substitute Ti^{4+} ions in the lattice or form surface species, such as CuO, Cu_2O, or metallic Cu [11]. These modifications create additional electronic states and extend light absorption into the visible region, thereby significantly enhancing photocatalytic hydrogen production [12–14]. While Cu-modified TiO_2 shows remarkable improvements, the reliance on TiO_2 as the main host still imposes limitations due to its intrinsic UV-driven activity. To further address the limitations of TiO_2, researchers have turned to lanthanum-based semiconductors, which possess tunable band structures, high electronic flexibility, and favourable optical properties.

Lanthanum has been reported to enhance photocatalytic efficiency by promoting charge separation through localized electric fields, acting as an electron trap, and improving surface adsorption via interactions between its f orbitals and Lewis base groups [15].

Within this class, lanthanum orthoferrite ($LaFeO_3$) has emerged as a highly promising photocatalyst. It is a p-type perovskite oxide, structurally stable, non-toxic, and composed of earth-abundant elements, making it environmentally and economically attractive for large-scale applications [16–18]. A key advantage of $LaFeO_3$ lies in its relatively narrow band gap (2.0-2.5 eV), which enables efficient visible-light absorption and provides a clear benefit over wide-band-gap semiconductors such as TiO_2 [19,20]. Structurally, $LaFeO_3$ crystallizes in an orthorhombic perovskite phase consisting of corner-sharing FeO_6 octahedra and La^{3+} cations are twelve-fold coordinated [21]. This arrangement contributes to its excellent crystallinity, stability, and favourable electronic characteristics, including variable valence states and defect chemistry [22,23]. Such features not only enable band-gap engineering but also facilitate catalytic redox reactions.

$LaFeO_3$ can be synthesized via scalable methods such as sol-gel processing, combustion, and hydrothermal routes [16–18]. These methods allow control over particle size, morphology, and surface area, which strongly influence its photocatalytic activity. Consequently, $LaFeO_3$ has found application in diverse areas such as pollutant degradation, hydrogen generation, gas sensing, and energy storage [16,17].

Despite these advantages, $LaFeO_3$ also faces challenges that hinder its practical implementation. Its relatively low surface area, limited light-harvesting ability compared to narrower-gap materials, and high electron-hole recombination rates reduce its photocatalytic efficiency [24]. To address these issues, coupling $LaFeO_3$ with other semiconductors has been widely investigated. In particular, $LaFeO_3/TiO_2$ composites have demonstrated synergistic effects, with improved charge separation and extended light absorption, leading to superior performance in both hydrogen evolution and organic pollutant degradation [25,26].

The synthesis route plays a crucial role in determining the structure, morphology, and performance of semiconductor composites. Conventional approaches, such as sol-gel, self-assembly, and impregnation followed by calcination, are effective but often involve expensive reagents and generate significant liquid waste, raising economic and environmental concerns [12,13,27–30]. To overcome these limitations, dry mechanical mixing methods, particularly ball milling, have been proposed as sustainable alternatives. These techniques reduce synthesis costs and environmental impact while maintaining effective interfacial contact between semiconductor phases. It is worth noting that, in this work, ball milling is employed under mild conditions (200 rpm, 1 min), significantly differing from high-energy ball milling approaches commonly reported in the literature. The adopted parameters, based on previous literature findings of some of the authors [14,26], are intentionally selected to promote intimate mixing between components while preserving the original crystal structure and avoiding the formation of excessive defects.

Building on this approach, the development of ternary systems combining Cu_xO, TiO_2, and $LaFeO_3$ offers a new pathway to synergistically harness the benefits of each component. TiO_2 provides stability and well-understood surface chemistry; Cu_xO introduces visible-light activity and strong redox behaviour; $LaFeO_3$ contributes broad visible-light absorption and structural tunability. Fig. 1 reports a schematic band alignment of Cu_xO (CuO/Cu_2O), TiO_2, and $LaFeO_3$ relative to the water redox potentials, based on literature information [4,12–14,19]. Arrows illustrate possible charge transfer pathways, showing how photogenerated electrons and holes can migrate between semiconductors, enhancing charge separation, reducing recombination, and promoting redox reactions. This ternary $Cu_xO/TiO_2/LaFeO_3$ system is thus expected to extend light absorption, enhance charge separation, and improve photocatalytic hydrogen generation efficiency through the photoreforming of sacrificial agents. In addition, Table 1 summarizes the key features of TiO_2, $LaFeO_3$, and Cu_xO (CuO/Cu_2O), and their combined heterojunction as photocatalysts.

In this work, both Cu(I) oxide and Cu(II) oxide were incorporated for the first time along with $LaFeO_3$ to evaluate the role of copper's oxidation state in determining photocatalytic behaviour. A systematic study was conducted, beginning with the evaluation of the single components, followed by binary systems, and finally the ternary composite. This stepwise approach provided insight into the synergistic interactions among the semiconductors. The ternary catalysts were then optimized to identify the most effective composition for hydrogen generation. Comprehensive characterization was performed to investigate the morphology, crystallinity, and electronic structure of the materials, while photocatalytic performance was evaluated under both UV and visible-light irradiation. Additionally, the effects of operational parameters, including reaction temperature, catalyst loading, and sacrificial agent type, were analyzed for the optimized catalyst.

2. Experimental part

2.1. Materials

TiO_2 (anatase nanopowder, 21 nm primary particle size) and CuO

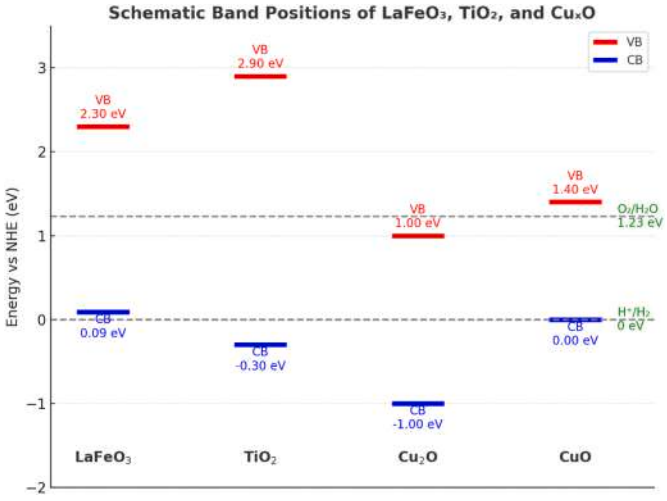

Fig. 1. Schematic band diagram of TiO_2, $LaFeO_3$, and Cu_xO (CuO/Cu_2O), showing their conduction and valence band positions relative to the water redox potentials [4,12–14,19].

Table 1
Band gaps, advantages, limitations, and applications of TiO_2, $LaFeO_3$, and Cu_xO (CuO/Cu_2O), and their combined heterojunction as photocatalysts.

Photocatalyst	Band Gap (eV)	Advantages	Limitations	Applications	Refs
TiO_2	~3.0–3.2	Abundant, low cost, stable, non-toxic	Only UV-active, fast e^-/h^+ recombination	Water splitting, pollutant degradation	[4]
$LaFeO_3$	~2.0–2.5	Visible-light absorption, tunable perovskite structure, non-toxic	Low surface area, high recombination, moderate activity	Pollutant degradation, hydrogen evolution, gas sensing	[19]
CuO/Cu_2O	~1.2–2.0	Strong visible-light absorption, good redox activity	Photocorrosion, stability issues	Hydrogen evolution, CO_2 reduction	[12–14]
$Cu_xO/TiO_2/LaFeO_3$ (ternary)	3.29–3.3	Synergistic charge separation, broad solar absorption, low-cost synthesis (ball milling)	Still under development, optimization required	Hydrogen generation via photoreforming, organic pollutant degradation	Present work

(nanopowder, <50 nm particle size) were purchased from Sigma Aldrich and used as received. $LaFeO_3$ was synthesized by citrate autocombustion method in nanopowder form [26,31]. Cuprous oxide (Cu_2O, powder), Glycerol (>99%), Glucose, Methanol (99.9%, for analysis) were purchased from Carlo Erba Reagents. All reagents were used as received. Doubly glass–distilled water was used throughout this study.

2.2. Photocatalyst preparation

The preparation of the binary and ternary photocatalytic materials was initially carried out through manual mixing of the powders, in which fixed amounts of TiO_2, $LaFeO_3$ and either CuO or Cu_2O were mixed and homogenized using a mortar and pestle. Selected samples were subsequently subjected to ball milling in a planetary mill (PM100, RETSCH) equipped with an agate jar and balls. The milling was performed at a rotation speed of 200 rpm for 1 min. These conditions were chosen based on prior optimization studies, previously reported in our earlier work [32], where the influence of milling parameters (i.e., milling time and rotation rate) on the material properties was systematically investigated and the optimal conditions were identified. Accordingly, the optimized parameters were directly adopted in the present study. Specifically, the samples exhibiting the best photocatalytic performance were chosen to evaluate the effect of the ball milling process.

2.3. Photocatalytic hydrogen generation

The reactor employed for the experimental tests is a glass annular batch reactor (V = 0.3 L) [32]. A high pressure Hg lamp is adopted as radiation source for the experiments; the specific powers of the lamp, mainly emitting at 305, 313 and 366 nm in UV range, and at 404.7 nm and 435.8 nm in the visible range, were calculated following a well-established protocol, as reported in literature [33]. The obtained values are $6.08 \cdot 10^{-7}$ E s^{-1}, $2.05 \cdot 10^{-6}$ E s^{-1}, $1.18 \cdot 10^{-6}$ E s^{-1}, $2.96 \cdot 10^{-7}$ E s^{-1}, and $1.97 \cdot 10^{-6}$ E s^{-1}, respectively (total radiant power equal to 2 W). For each experiment, 0.25 L of an organic solution (0.05 M) have been added to the reactor. Different sacrificial agents (i.e., glycerol, glucose, methanol) have been employed to evaluate their effect on the photocatalytic hydrogen evolution. An inertisation procedure is then started by inserting Ar in the reactor through a gas diffusor inside the solution for 40 min before the photocatalytic experiment (0.3 L min^{-1}). Then the catalyst (0.2 g L^{-1}) is added to the system, and the lamp is switched on. The temperature was kept constant at selected values in the range of 35–90°C by means of a cooling jacket. Photocatalytic hydrogen production under visible light radiation has also been analyzed for binary catalyst as well as for the best conditions in the ternary catalyst. UV filtering was achieved by introducing a $NaNO_2$ (0.5 M) solution into the lamp jacket, effectively blocking radiation with wavelengths below 400 nm [34]. Hydrogen evolution was quantified by collecting gas samples at predetermined time intervals using 1 L Tedlar sampling bags positioned at the outlet of the argon stream. The collected samples were subsequently analyzed by gas chromatography (Agilent 7820A) equipped with an HP-PLOT Molesieve 5A column (Agilent) and a thermal conductivity detector (TCD), with argon employed as the carrier gas.

2.4. Physicochemical characterization

Fourier Transform Infrared (FTIR) analyses of the samples were carried out using the attenuated total reflection (ATR) accessory of an FTIR Spectrometer Hyperion II Vertex 80v PL II. Raman spectroscopy was conducted using a Via Confocal Raman Microscope at a wavelength of 532 nm. Scanning electron microscopy was performed using FEI Nova NanoSEM 650. The samples were coated with a layer of Au/Pd (gold/palladium) before the SEM analyses. Energy-dispersive X-ray spectroscopy (EDS) was used for elemental mapping of the samples. A Thermo Scientific Phenom XL G2 Scanning Electron Microscope was used for the EDS mapping and analyses. Transmission electron microscopy (TEM) and selected area electron diffraction (SAED) were conducted using a FEI Titan microscope operated at 300 kV to investigate the morphology and crystalline nature of the samples. The metal concentrations in the samples were measured using a Thermo Scientific iCAP 7600 Inductively Coupled Plasma Optical Emission Spectroscopy (ICP-OES) analyser. Prior to the analyses, the powder samples were added to a 10 mL acid mixture (concentrated HNO_3, concentrated HCl, and concentrated H_2SO_4 with a volumetric ratio of 1:3:12). This was followed by digestion in a CEM Mars 6 microwave digestion system at a temperature of 210 ∘C for 30 min. After the digestion, the samples were diluted with deionized water and ready for ICP-OES analyses. The relative percentage weights of the metals in each of the samples were then calculated from the concentration values. UV–visible diffuse reflectance spectra (UV–vis DRS) were recorded using a Shimadzu UV-2600 spectrophotometer equipped with an integrating sphere, covering the wavelength range of 200–800 nm. The Photoluminescence (PL) spectroscopy was performed using a PerkinElmer LS 55 Luminescence Spectrometer at an excitation wavelength of 280 nm. The crystallinity of the samples was characterized using an Empyrean PANalytical X-ray diffractometer with Cu Kα radiation (λ = 1.5406 Å), operated at 40 kV and 40 mA. Data were acquired over a 2θ range of 20°–70°, with a step size of 0.02°. Debye-Scherrer formula (1) below was used to calculate the crystallite sizes:

$$L = \frac{K\lambda}{B\cos\theta} \quad (1)$$

where K is the Scherrer constant (0.89), λ is the wavelength of the XRD instrument, θ is the diffraction angle, B is the peak full width at half maximum of the intensity plotted against the 2θ profile, and L is the crystallite size in nm [35]. X-ray photoelectron spectroscopy (XPS) measurements were performed using a PHI VersaProbe 5000 scanning XPS system equipped with a Mg Kα radiation source (1254 eV). The spectra were analyzed using CASA XPS software.

3. Results and discussion

3.1. Material characterization

The results from the FTIR analyses are shown in Fig. S1. The characteristic bands for TiO_2, $LaFeO_3$, CuO and Cu_2O are highlighted and show strong agreement with the literature [36–38]. For the ternary samples (i.e., (93%wt.)TiO_2/(2%wt.)Cu_2O/(5%wt.)$LaFeO_3$ and (86.14%wt.)TiO_2/(10%wt.)CuO/(3.86%wt.)$LaFeO_3$), the OH stretch bands of TiO_2 are present, but the bands from the other components were not detected (owing to the much smaller weight percentages of the other powders and to the other powders being highly dispersed as very small particles). Fig. S2 shows the Raman spectra of the samples. The peaks identified for TiO_2, $LaFeO_3$, CuO and Cu_2O have been confirmed from literature [38–40]. Additionally, both ternary samples exhibited Raman peaks at 510−520 cm^{-1} attributable solely to TiO_2, likely due to its predominant weight fraction in the composites.

Fig. 2 presents the SEM images of the analyzed samples. The ternary composites (Fig. 2(A–G, B, H)), TiO_2 (Fig. 2(D–J)), and CuO (Fig. 2 (E–K)) exhibit a spongy morphology, with CuO displaying comparatively larger particles. In contrast, $LaFeO_3$ (Fig. 2(C–I)) shows a layered, slate-like structure with each slate comprising many small particles lumped together. Lastly, the Cu_2O (Fig. 2(F–L)) powders appear as coarse, compact particles and exhibit the largest size among all examined materials.

The TEM and high-resolution TEM (HRTEM) images shown in Fig. 3 provide detailed structural insights into the bare metal oxides and their composites. Fig. 3(a and b) depict TiO_2 nanoparticles, showing well-dispersed nanosized particles with clear lattice fringes indexed to the (101) plane with d-spacings of 0.359 nm and 0.326 nm, characteristic of anatase TiO_2 [41]. In Fig. 3(c and d), $LaFeO_3$ particles exhibit slightly larger particles with a d-spacing of 0.391 nm, attributed to the (101) reflection of orthorhombic $LaFeO_3$ [42]. Fig. 3(e and f) depict CuO, where the lattice spacing of 0.232 nm is indexed to the (200) plane, confirming the presence of monoclinic CuO [43]. Similarly, Cu_2O shown in Fig. 3(g and h) displays well-defined nanoparticles with a measured interplanar distance of 0.213 nm, assignable to the (200) planes of cubic Cu_2O. The composite illustrated in Fig. 3(i and j) for the (93%wt.) TiO_2/(2%wt.)Cu_2O/(5%wt.)$LaFeO_3$ sample demonstrates coherent interfaces among the constituents, with measured spacings of 0.289 nm for $LaFeO_3$ (121) and 0.357 nm for TiO_2 (101), indicating strong interfacial contact which can be beneficial for charge transfer. Whereas, the (86.14%wt.)TiO_2/(10%wt.)CuO/(3.86%wt.)$LaFeO_3$ composite in Fig. 3 (k and l) exhibited coexisting lattice fringes of TiO_2 (0.356 nm, (101)) and CuO (0.239 nm, (200)), highlighting successful heterojunction formation. The combination of phases, as confirmed by lattice spacing and selected area electron diffraction (SAED) patterns, confirms the multi-phase composition.

Fig. 4 shows the EDS elemental mapping of the samples. For each sample, the elements corresponding to its constituent components were detected. The relative weights of the metal elements in each sample were also presented in Table S1. The percentage weight values obtained from the ICP-OES analyses are comparable to the values obtained from EDS and from stoichiometric calculations.

The optical properties of the bare and nanocomposite samples were studied using UV–vis DRS, as presented in Fig. 5 (a). The spectra show that TiO_2 exhibited the highest reflectance, indicating limited visible light absorption due to the relatively wide band gap of 3.34 eV. Whereas $LaFeO_3$, CuO and Cu_2O based nanocomposites showed significantly lower reflectance, indicating improved visible light absorbance. This improvement was attributed to the synergistic effect of $LaFeO_3$, CuO and Cu_2O and efficient charge transfer through the formed heterojunctions. Fig. S3 shows the Tauc plots of the as-prepared samples. The optical bandgap energies were estimated by extrapolating the linear portion of the $(\alpha h\nu)^{1/n}$ vs. photon energy ($h\nu$) curves to the x-axis intercept. Fig. 5 (b) displays the PL spectra for the samples containing TiO_2. The intensity of the spectra decreases with the proportion of TiO_2 in the samples. Bare TiO_2 has the highest intensity, followed by (93%wt.)TiO_2/(2%wt.) Cu_2O/(5%wt.)$LaFeO_3$, and then (86.14%wt.)TiO_2/(10%wt.)CuO/ (3.86%wt.)$LaFeO_3$.

Similarly, the peak positions decrease with with the proportion of TiO_2 in the samples. The peak of bare TiO_2 occurs at 398 nm, followed by (93%wt.)TiO_2/(2%wt.)Cu_2O/(5%wt.)$LaFeO_3$ at 397 nm, and then (86.14%wt.)TiO_2/(10%wt.)CuO/(3.86%wt.)$LaFeO_3$ at 396 nm. Emission peaks were not detected for bare $LaFeO_3$, bare CuO, and bare Cu_2O at the excitation wavelength of 280 nm.

The XRD patterns of the nanocomposites and their corresponding bare samples are depicted in Fig. 6. $LaFeO_3$ exhibited peaks at 22.9°, 32.6°, 40.0°, 46.6°, 52.4°, 53.6°, 57.8°, and 67.7°, which were assigned to (101), (121), (220), (202), (141), (311), (240), and (242) diffraction planes, respectively. Accordingly, $LaFeO_3$ exhibited a single-phase orthorhombic perovskite structure matching the JCPDS card number 37-1493 [26]. In the bare TiO_2 sample and composite samples, the presence of anatase TiO_2 (JCPDS No. 21-1272), and rutile TiO_2 (JCPDS No. 21-1276) is clearly observed, where the anatase phase is confirmed by prominent peaks at 25.5° and 48°, corresponding to the (101) and (200) planes, respectively while the rutile phase exhibits a peak at 27.7° attributed to (110) plane [44]. In the XRD patterns of the nanocomposites, characteristic peaks of CuO were observed in the (86.14% wt.)TiO_2/(10%wt.)CuO/(3.86%wt.)$LaFeO_3$ sample at 35.8° and 38.9° assigned to (002) and (200) planes, indicating the presence of crystalline CuO [45]. In contrast, Cu_2O peaks were not detected in the (93%wt.) TiO_2/(2%wt.)Cu_2O/(5%wt.)$LaFeO_3$ composite, likely due to its low content, making it below the detection limit of XRD [32]. Furthermore, no appreciable changes were observed in the XRD patterns of either ternary composite before and after the photocatalytic reaction (Fig. S4), suggesting that the crystalline structure of the materials was preserved under the investigated reaction conditions. The crystallite size of all samples calculated using Sherrer's equation from the XRD data are summarized in Table S2. The ternary composite samples exhibit smaller crystallite sizes of 16.26 and 16.35 nm compared to their individual components, which is attributed to the disorder in the lattice structure and the creation of more grain boundaries upon nanocomposite formation [46].

The elemental composition and oxidation states of the samples were analyzed using XPS. The survey spectra in Fig. 7 (a) confirm the presence of Ti 2p, Cu 2p, Fe 2p, La 3d, and O 1s. The high-resolution Ti 2p spectrum of TiO_2 (Fig. 7 (b)) exhibited doublet peaks at 458.4 and 463.9 eV corresponding to Ti $2p_{3/2}$ and Ti $2p_{1/2}$ spin-orbitals of Ti^{4+} (TiO_2), while peaks at 457.7 and 462.3 were attributed to Ti $2p_{3/2}$ and Ti $2p_{1/2}$ of Ti^{3+} (Ti_2O_3) [47]. Additionally, a shift of approximately 1.1 eV toward higher binding energy (BE) was observed in the nanocomposites, which could be ascribed to a decrease in Ti electron density due to the formation of heterojunctions, where Cu or $LaFeO_3$ acts as an electron withdrawing component [48]. In Fig. 7 (c), the main Cu $2p_{3/2}$ peak appeared near 933 eV, which is consistent with Cu^{2+}, while a weak satellite around 942 eV further confirmed the Cu^{2+} state [49]. Compared to the spectra of bare CuO and Cu_2O, a slight shift in the peak position was observed in the composites, suggesting electronic interactions between Cu and $LaFeO_3$/TiO_2. This shift, along with the weak satellite intensity, indicates a coexistence of Cu^{+} and Cu^{2+} species [50]. The Cu 2p XPS spectrum of (86.14%wt.)TiO_2/(10%wt.)CuO/(3.86%wt.)$LaFeO_3$ reveals the presence of Cu^{+} rather than Cu^{2+} as observed in bare CuO which was attributed to interfacial electron transfer from the CB of TiO_2 to Cu^{2+} sites upon heterojunction formation, resulting in the partial reduction of Cu^{2+} to Cu^{+}. This phenomenon has been previously reported in TiO_2/CuO composite systems in several work [51–53]. In $LaFeO_3$, both La 3d and Fe 2p exhibited a 3+ oxidation state as shown in Fig. 7(d–e). Specifically, La $3d_{5/2}$ and La $3d_{3/2}$ were observed at 833.1 and 849.9 eV, respectively [37], while Fe 2p peaks at 710.1 and 723.4 eV were assigned to Fe $2p_{3/2}$ and Fe $2p_{1/2}$, respectively. However, due to the low loading of Cu, Fe and La, their signals were not detected in

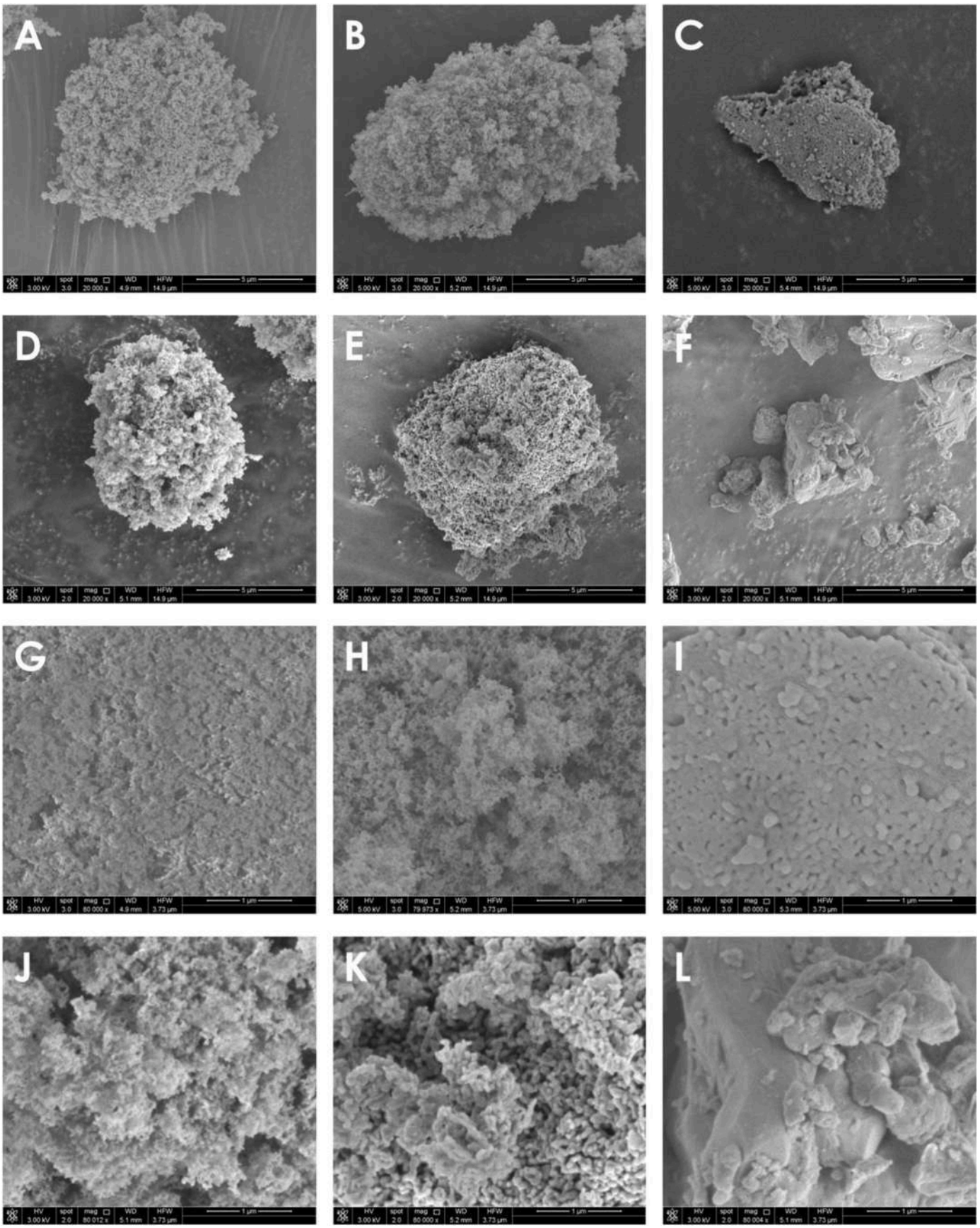

Fig. 2. SEM images of the powders at different magnifications. (A, G) (93%wt.)TiO_2/(2%wt.) Cu_2O/(5%wt.)$LaFeO_3$; (B, H) (86.14%wt.)TiO_2/(10%wt.)CuO/(3.86% wt.)$LaFeO_3$; (C, I) bare $LaFeO_3$; (D, J) bare TiO_2; (E, K) bare CuO; (F, L) bare Cu_2O.

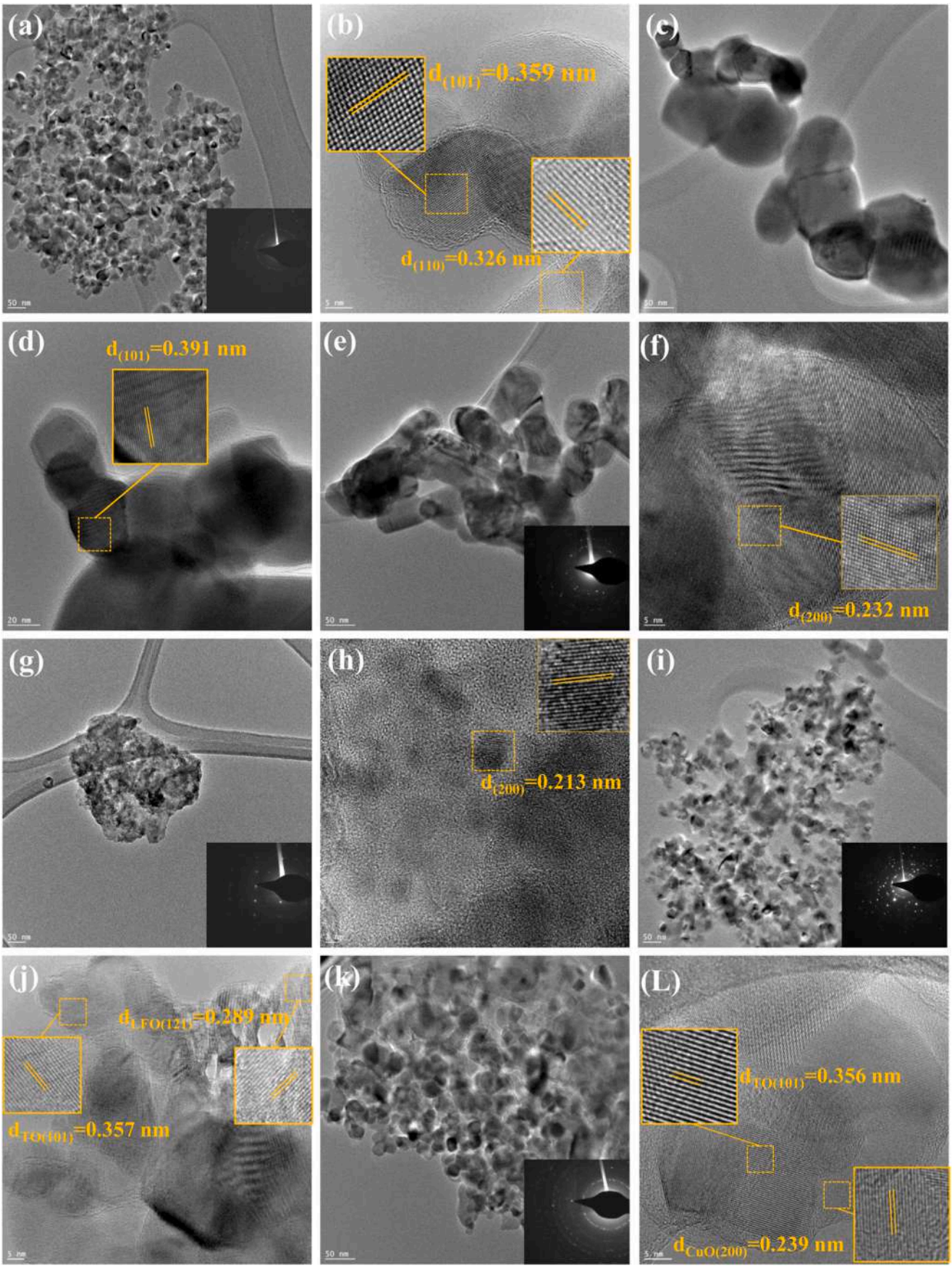

Fig. 3. HR-TEM images and SAED patterns of the samples: (a-b) TiO_2, (c-d) $LaFeO_3$, (e-f) CuO, (g-h) Cu_2O, (i-j) (93%wt.)TiO_2/(2%wt.)Cu_2O/(5%wt.)$LaFeO_3$ and (k-l) (86.14%wt.)TiO_2/(10%wt.)CuO/(3.86%wt.)$LaFeO_3$.

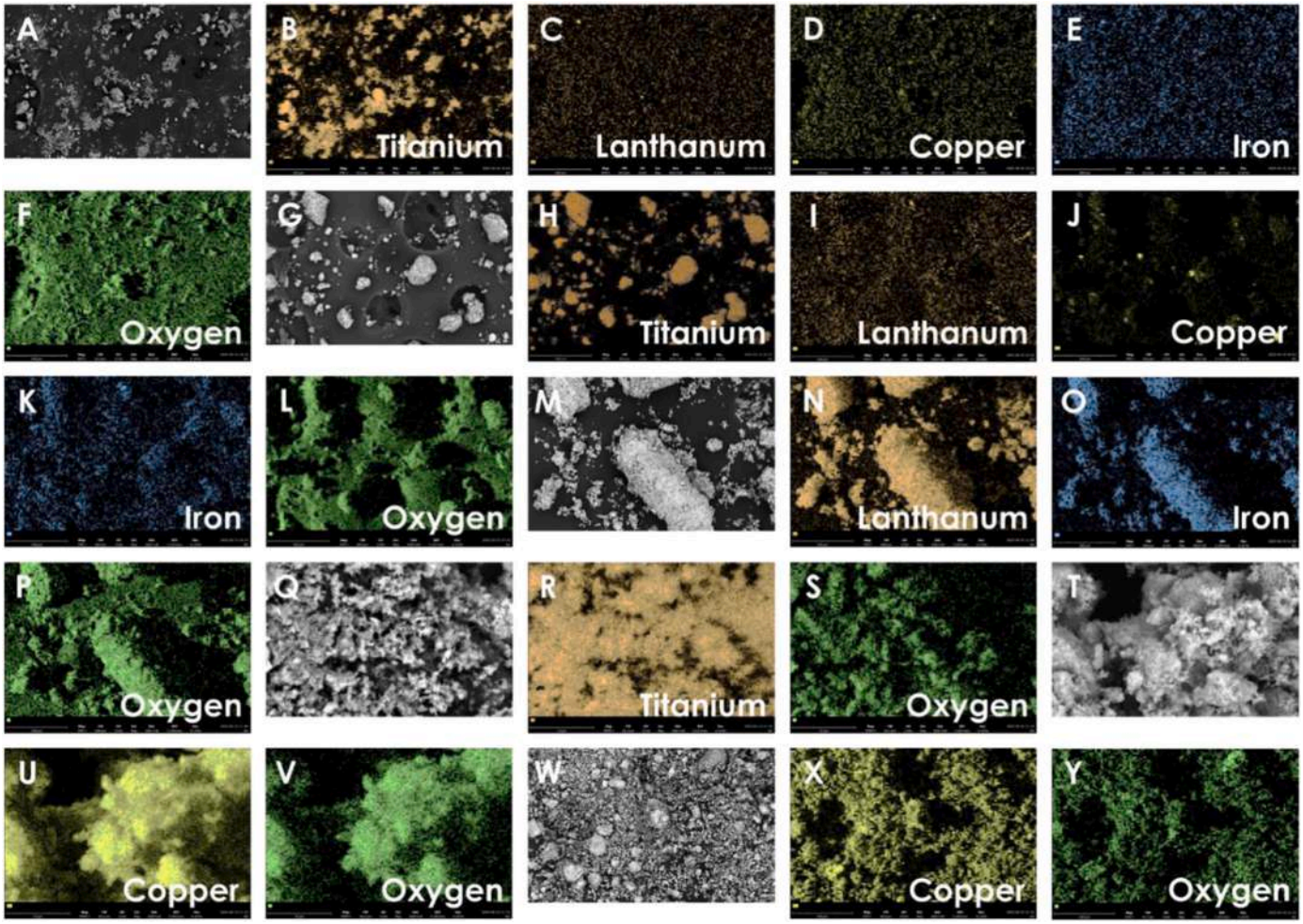

Fig. 4. EDS mapping analysis of the powders. (A-F) (93%wt.)TiO_2/(2%wt.)Cu_2O/(5%wt.)$LaFeO_3$; (G-L) (86.14%wt.)TiO_2/(10%wt.)CuO/(3.86%wt.)$LaFeO_3$; (M – P) bare $LaFeO_3$; (Q-S) bare TiO_2; (T-V) bare CuO; (W–Y) bare Cu_2O.

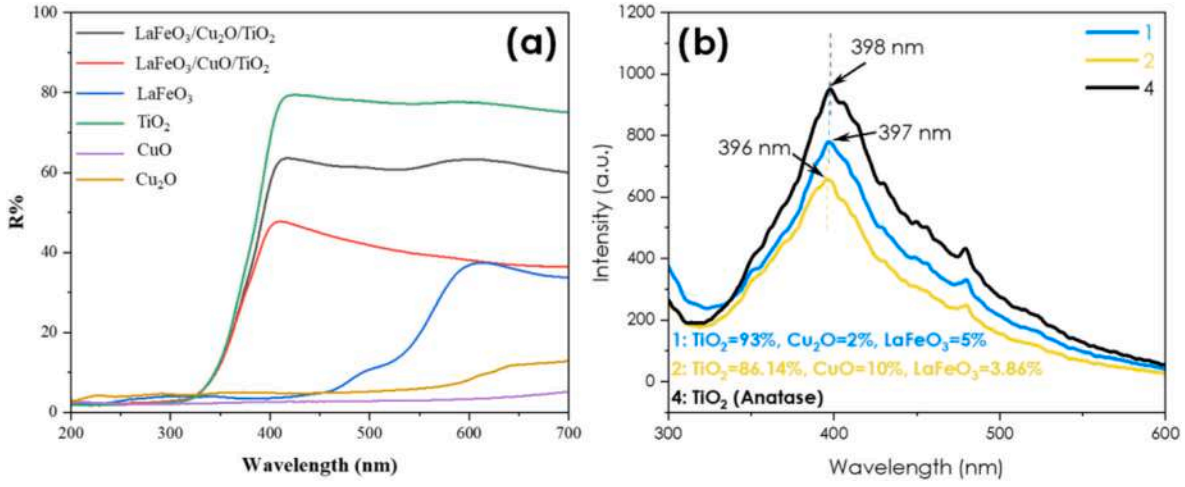

Fig. 5. (a) UV-visible diffuse reflectance spectra of the nanocomposites and bare samples and (b) Photoluminescence spectra of the powders. Sample labels are as follows. **1:** (93%wt.)TiO_2/(2%wt.)Cu_2O/(5%wt.)$LaFeO_3$; **2:** (86.14%wt.)TiO_2/(10%wt.)CuO/(3.86%wt.)$LaFeO_3$; **4:** bare TiO_2.

the nanocomposites. The O 1s spectrum of $LaFeO_3$ in Fig. 7 (f) showed a peak corresponding to lattice oxygen $O_{L\ (perovskite)}$ from the perovskite structure. All samples exhibited peaks around 531 eV, attributed to O^{2-} in Ti–O, Cu–O or Fe–O bonds. Additionally, peaks associated with adsorbed H_2O were detected around 532 eV in CuO, $LaFeO_3$ and (93% wt.)TiO_2/(2%wt.)Cu_2O/(5%wt.)$LaFeO_3$ samples, whereas peaks related to surface OH species were observed around 533 eV for Cu_2O, TiO_2 and (86.14%wt.)TiO_2/(10%wt.)CuO/(3.86%wt.)$LaFeO_3$, respectively [54].

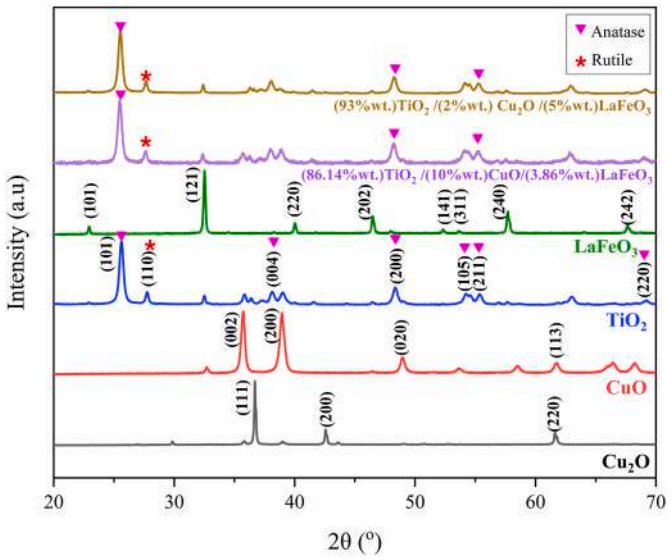

Fig. 6. XRD diffraction patterns of the nanocomposites and bare samples.

3.2. Photocatalytic hydrogen generation

3.2.1. Preliminary results: single and binary components

Preliminary tests were conducted to compare the hydrogen production in the presence of bare TiO_2, bare Cu_2O or CuO, and bare $LaFeO_3$. No hydrogen generation was recorded in the presence of bare Cu_2O as well as in the presence CuO and $LaFeO_3$, while a low activity was observed for bare TiO_2 (lower than 500 μmol/g h) [55,56]. The reason can be ascribed to the unsuitable band gap positions of CuO and $LaFeO_3$ [26,57], and low photostability in aqueous solution, especially for the copper-based oxides [58,59]. For the binary photocatalysts, only (3.86% wt.)$LaFeO_3/TiO_2$, (10%wt.)CuO/TiO_2, and (1%wt.)Cu_2O/TiO_2 demonstrated a non-negligible photocatalytic hydrogen generation, as clearly indicated in Fig. 8.

The relative ratios between the semiconductors in the CuO/TiO_2, and Cu_2O/TiO_2 systems were selected based on previous studies [32,60], in which the effect of copper oxide loading on photocatalytic performance was systematically investigated and the optimal compositions were identified. Similarly, the $LaFeO_3/TiO_2$ ratio was chosen based on a preliminary optimization study [26], which identified (3.86%wt.) $LaFeO_3/TiO_2$ as the most effective composite material. Among the binary systems tested, (3.86%wt.)$LaFeO_3/TiO_2$ and (10%wt.)CuO/TiO_2 demonstrated the highest reactivity under the UV + Visible light range, probably due to the reduction of the electron-hole recombination rate [26]. Conversely, the experiments conducted under the visible light range demonstrated a non-negligible activity only in the case of Cu_2O/TiO_2 photocatalyst, as confirmed by previous literature findings [32].

3.2.2. Ternary systems

The analysis of ternary components has started from the basis of the previously mentioned results for binary components. Specifically, the ratio among the three components of the catalyst has been varied, keeping the catalyst load constant (i.e., 0.2 g L^{-1}). Different ratios of the semiconductors have been evaluated, as it will be shown in ternary diagrams, to better clarify the ratio and the average H_2 production.

3.2.2.1. $CuO/LaFeO_3/TiO_2$. The effect of the increase of cupric oxide and lanthanum ferrites in the catalyst's composition has been evaluated. To evaluate the effect of the single component variation, a fixed quantity of the second co-catalyst has been fixed during the procedure. The quantities have been set as 10% for CuO and 3.86% for $LaFeO_3$, based on the previous results. The data collected from binary and ternary systems at fixed proportions allowed us to assess whether manual mixing of the materials has any effect on the productivity of the process. Fig. 9 shows

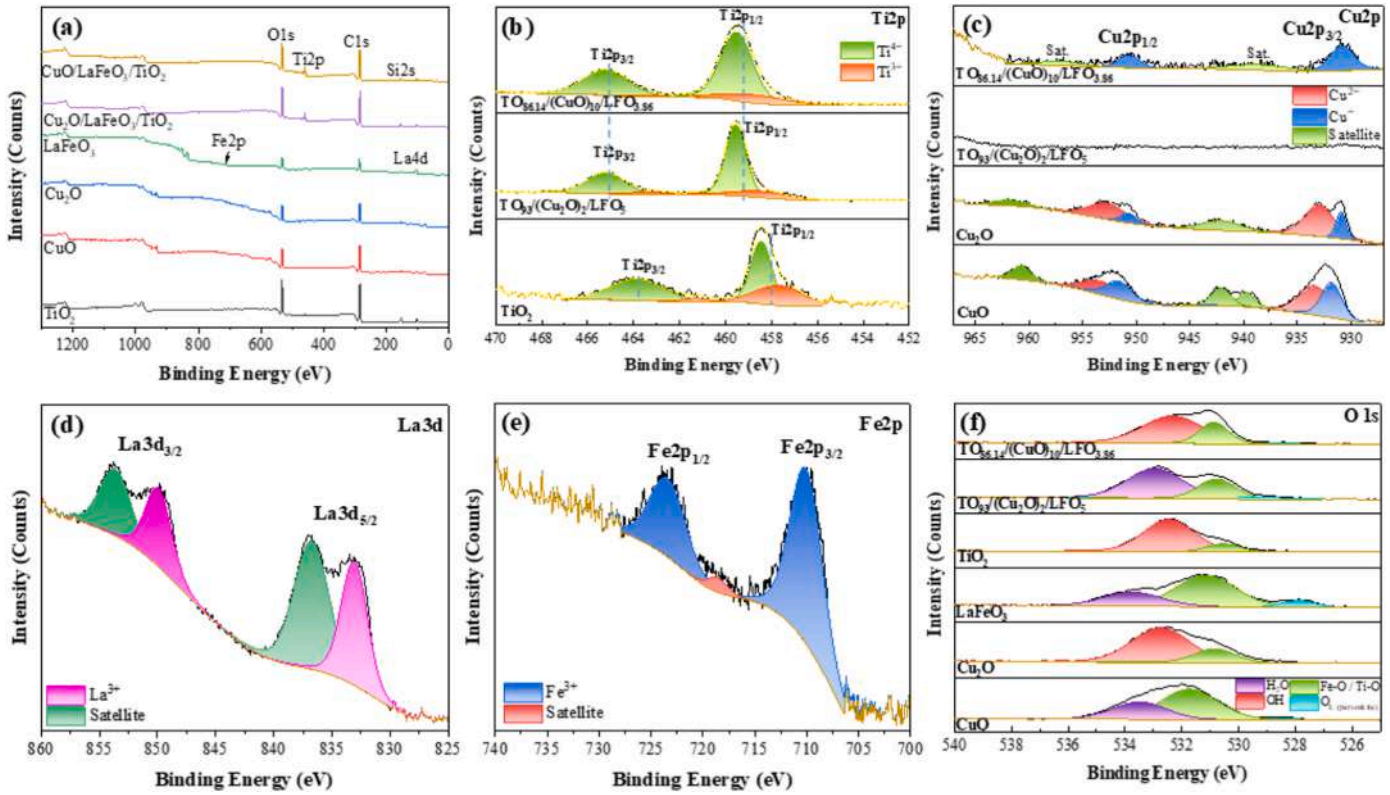

Fig. 7. XPS spectra: (a) survey scans, (b) Ti 2p, (c) Cu 2p, (d) La 3d, (e) Fe 2p and (f) O 1s.

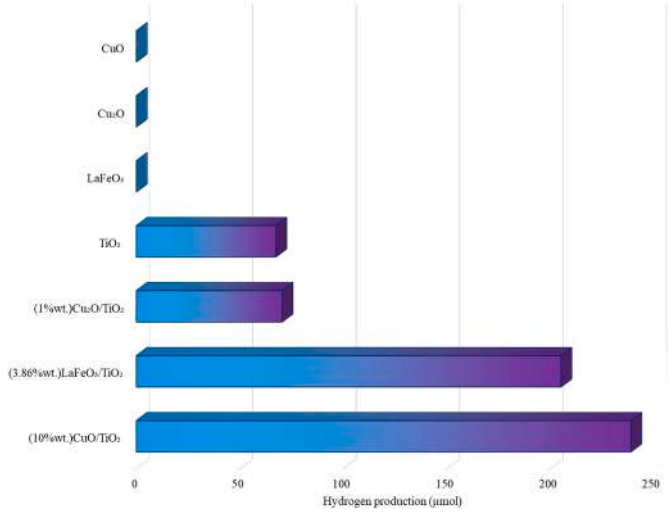

Fig. 8. Hydrogen production after 3 h of irradiation at varying the photocatalyst adopted under UV + visible light radiation. Experimental conditions: C_{cat} = 0.2 g L^{-1}; [Glycerol] = 0.05 M; V = 0.25 L; pH ~ 5.5.

the main results. As indicated in the figure, in contrast to the previously mentioned consideration, the results demonstrated a hydrogen productivity (yellow dot) about 3.5-fold higher than the productivity obtained in the presence of the binary systems under the same conditions (i.e., (3.86%wt.)$LaFeO_3/TiO_2$ and (10%wt.)CuO/TiO_2), thereby revealing a pronounced synergistic effect among the materials. The enhanced hydrogen evolution performance of the composite can be rationalized based on its structural and morphological features observed through HRTEM and SAED analyses (See Fig. 3(k and l)), from which strong evidence of successful heterojunction formation is obtained. The intimate interfacial contact among the semiconductor phases could facilitate more efficient charge separation and transfer, thereby reducing the recombination rate (as observed by PL spectra reported in Fig. 5 (b)). As indicated in the inset of Fig. 9, the best conditions were identified at 86.14%wt. of TiO_2, 10%wt. of CuO and 3.86%wt. of $LaFeO_3$, with a maximum amount of the produced hydrogen equal to 828 μmol after 3 h of irradiation under UV + visible irradiation.

3.2.2.2. $Cu_2O/LaFeO_3/TiO_2$. To evaluate the effects of the single component amount, a fixed quantity of the second co-catalyst was first fixed through the procedure. The quantities have been set as 2% for Cu_2O and 3.86% for $LaFeO_3$ and the main result are shown in Fig. 10.

The choice of using different ratios with respect to the previously studied binary systems is due to the different hydrogen production rate. It can be argued that the addition of small amounts of Cu_2O leads to the formation of the heterojunction structure, thus improving hydrogen generation. In contrast, high contents of cuprous oxide reduce the light energy absorbed by TiO_2/Cu_2O nanoparticles of TiO_2 due to the excess coverage of the titanium dioxide surface and the formation of higher content of Cu^+ during the reaction. As indicated in the inset of Fig. 10, the best conditions were identified at 92.5%wt. of TiO_2, 2.5%wt. of Cu_2O and 5%wt. of $LaFeO_3$, with a maximum amount of the produced hydrogen equal to 338 μmol after 3 h of irradiation under UV + visible irradiation.

Similar to the previous results, the superior photocatalytic hydrogen production observed for the composite with respect to the bare photocatalysts can be correlated with the structural characteristics revealed by HRTEM analysis. Indeed, as shown in Fig. 3(i and j), the composite exhibits coherent interfaces among the three phases, indicative of effective heterojunction formation, thus facilitating charge separation and interfacial charge transfer across the different semiconductors. Furthermore, the intimate contact among the constituent phases probably plays a crucial role in suppressing electron–hole recombination (confirmed by PL spectra reported in Fig. 5 (b)), thereby enhancing the overall photocatalytic efficiency.

Considering Figs. 9 and 10, it is clear that the materials present a different reactivity in terms of hydrogen generation, with CuO-based composites resulting in the most efficient. However, after the first hour of irradiation, the system involving $Cu_2O/LaFeO_3/TiO_2$ shows a more stable behaviour (Fig. S7), thus corresponding to a more stable photocatalytic material.

3.3. *Effect of the ball milling*

The obtained powders appear uniform; however, during the tests, the ball milled photocatalyst containing cupric oxide (i.e., (86.14%wt.) TiO_2/(10%wt.)CuO/(3.86%wt.)$LaFeO_3$) showed inconsistent results, meaning that the uniformity of the catalyst was compromised. It is important to note that this behavior is not related to limitations of the ball milling process itself, which is generally recognized as a scalable and reproducible technique, but rather to the intrinsic properties of the material. Specifically, this could be attributed to a higher hygroscopicity of the cupric oxide with respect to the cuprous oxide. If this holds, some studies [61] reported the usage of D-sorbitol as a milling agent. Sorbitol is commonly used for its high hygroscopicity in food preservation.

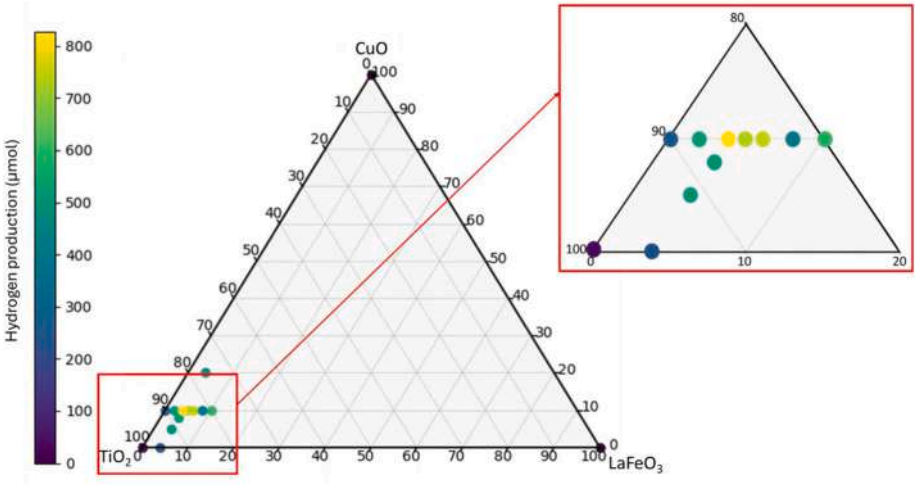

Fig. 9. Hydrogen produced amount after 3 h of irradiation at varying the ternary photocatalyst employed. Experimental conditions: C_{cat} = 0.2 g L^{-1}; [Glycerol] = 0.05 M; V = 0.25 L; pH ~ 5.5; UV + Visible light radiation.

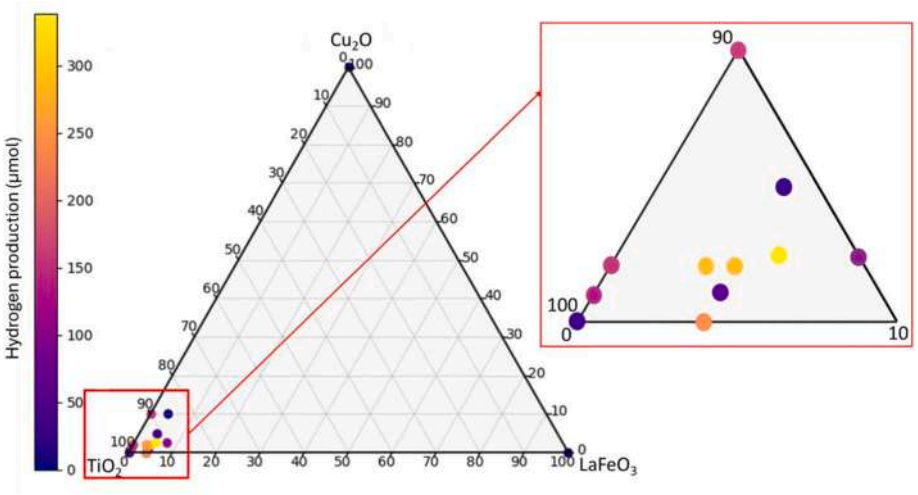

Fig. 10. Hydrogen produced amount after 3 h of irradiation at varying the ternary photocatalyst employed. Experimental conditions: C_{cat} = 0.2 g L^{-1}; [Glycerol] = 0.05 M; V = 0.25 L; pH ~ 5.5; UV + Visible light radiation.

Therefore, it could be useful in controlling the interaction of cupric oxide with water in the atmosphere. Hence, the results on the sample (86.14%wt.)TiO_2/(10%wt.)CuO/(3.86%wt.)$LaFeO_3$ accounts only for an average behaviour after ball milling, while the inhomogeneity of the sample did not allow further tests due to the low reproducibility of the results.

By comparing the produced hydrogen amount in the presence of the "milled" and "unmilled" photocatalysts, it is clear that in the case of cupric-based materials the ball milling procedure lowers the photoactivity of the composites, accounting for 828 μmol in the case of manual mixing and 454 μmol in the case of ball milling (Table 2). Coupling this decrease with the low reproducibility of the results in the latter case, it has been decided to exclude the cupric-based ternary materials from the next experiments. On the other hand, when the ternary mixture containing Cu_2O has been tested after the ball milling procedure, an increase in the average H_2 production is shown, with an increase in the performance of 33.34% (Table 2). Furthermore, it is important to stress again that the stability of this system is far greater than that of the one with cupric oxide.

Based on these results, in the following sections the effect of the catalyst load, temperature and sacrificial agent on the hydrogen productivity will be discussed, focusing on the (93%wt.)TiO_2/(2%wt.)Cu_2O/(5%wt.)$LaFeO_3$ composite material prepared through the ball milling procedure.

3.3.1. *Effect of the sacrificial agent employed*

The (93%wt.)TiO_2/(2%wt.)Cu_2O/(5%wt.)$LaFeO_3$ composite prepared through ball milling was employed in the presence of different sacrificial agents for hydrogen generation. Glycerol, methanol, and glucose were chosen as the most reported sacrificial agents [30,62,63]. The results are reported in Table 3.

Table 2
Comparison of the hydrogen production after 3 h of irradiation in the presence of the ternary composites when the samples are prepared by simple mixing or through the ball milling procedure.

Composite material	Average Hydrogen amount after 3 h of irradiation (μmol)	
	Unmilled	Milled
(86.14%wt.)TiO_2/(10%wt.)CuO/(3.86%wt.)$LaFeO_3$	828	454[a]
(93%wt.)TiO_2/(2%wt.)Cu_2O/(5%wt.)$LaFeO_3$	338	440

[a] Average value obtained from different experiments in the same conditions. The experiments demonstrated a low reproducibility.

As indicated, the highest reactivity was obtained in the presence of glycerol, with a hydrogen amount about 4 times higher than methanol, and 2.5 times higher than glucose. The different behaviour is influenced by the nucleophilicity of the functional groups of their molecular structures, as well as their ability to adsorb onto the catalyst's surface [64–66]. The structure of the molecule can be the reason for the lower reactivity of glucose with respect to glycerol since the steric hindrance hinders the interactions with the photogenerated positive holes [67] (despite the presence of more electron-donor groups). Furthermore, concerning adsorption phenomena, glycerol likely forms bidentate (or even tridentate) complexes, whereas methanol tends to form weaker monodentate complexes [14].

According to Panagiotopoulou et al. [68], under inert atmosphere glycerol oxidation proceeds via a photo-reforming pathway in which the molecule is initially activated through dehydrogenation to glyceraldehyde and/or hydrogenolysis to propylene glycol (via acetol). These intermediates undergo subsequent dehydration, dehydrogenation, and decarbonylation steps, forming smaller oxygenated products such as glycoaldehyde, acetaldehyde, acetone, ethanol, and methanol. Progressive C–C bond cleavage leads to C_1 species (mainly CO), which, in the absence of O_2, is converted to CO_2 via the water–gas shift reaction, while photogenerated electrons reduce protons to H2. Overall, the process results in the conversion of glycerol into CO_2 and H_2, with slower kinetics and greater accumulation of intermediates compared to aerobic conditions.

3.3.2. *Effect of the catalyst load and sacrificial agent concentration*

The effects of the catalyst load have been evaluated by increasing the amount of composite by 0.2 g L^{-1} for each experiment. An increasing amount of hydrogen was produced upon increasing the catalyst load, with a maximum value of 2.52 mmol obtained after 3 h of irradiation when 0.8 g L^{-1} of photocatalyst were employed. Beyond this value, the slight decrease in the reactivity was motivated by the scattering effect exerted by the solid particles in the reaction medium [69]. The results

Table 3
Comparison of the hydrogen production after 3 h of irradiation in the presence of different organic compounds. Experimental conditions: C_{cat} = 0.2 g L^{-1}; [Organic compound] = 0.05 M; V = 0.25 L; pH ~ 5.5; T = 35°C; UV + Visible light radiation.

Organic compound	Average Hydrogen amount after 3 h of irradiation (μmol)
Methanol	100
Glycerol	440
Glucose	175

are shown in Fig. 11 (A).

Fig. 11 (B) reports the photocatalytic hydrogen generation at varying the concentration of organic compounds adopted during the experiment. As indicated, the maximum amount of hydrogen (i.e., ≈5 mmol within 3 h of irradiation) was obtained in the presence of 0.5 M glycerol. The reaction rate observed during the photocatalytic experiments at different organic concentrations is accurately represented by a Langmuir-Hinshelwood model [14]. This compound was chosen considering the drastic decline of glycerol price in recent years, representing 10% of the by-products generated during biodiesel production, which corresponds to a significant global oversupply [70,71].

3.3.3. Effect of the temperature

It is well known that photocatalytic activity is only slightly influenced by temperature, as electron-hole pair generation primarily depends on radiation intensity [72]. However, temperature can still be used to enhance photocatalytic activity by increasing the reaction rate, improving the desorption of products from the catalyst surface, and facilitating electron transfer from the valence band to higher energy levels in the presence of light irradiation [73,74]. The increase in reaction temperature in the presence of light irradiation, therefore, aids in forming electron-hole pairs that can initiate oxidation and reduction reactions, while helping the reactions compete more effectively with charge carrier recombination, as reported by various researchers. For this reason, some experimental tests were conducted by varying the reaction temperature between 35°C and 90°C, using glycerol as a sacrificial agent. As shown in Fig. 12 when the temperature increased from 35°C to 90°C, hydrogen production achieves a value about 3.6 times higher than that obtained at the lowest temperature, thus demonstrating the positive effect of temperature on the system. Control experiments performed under dark conditions at both 35°C and 90°C showed no detectable hydrogen production, confirming that H_2 evolution requires irradiation and that thermal effects alone do not contribute to the reaction.

3.3.4. Evaluation of the photocatalytic activity under visible light

A set of experiments was conducted under visible-light-only irradiation to assess the activity of the material when activated at wavelengths above 400 nm. As shown in Fig. 13, compared to the results obtained under full-spectrum illumination, the visible component alone leads to a hydrogen production of approximately 10% of that observed yield with the entire light spectrum. Nevertheless, when this result is compared to that of TiO_2, for which negligible activity in the visible range has been reported under similar conditions in a previous work of some of the authors [32] (data not shown), it is clear that the composite material

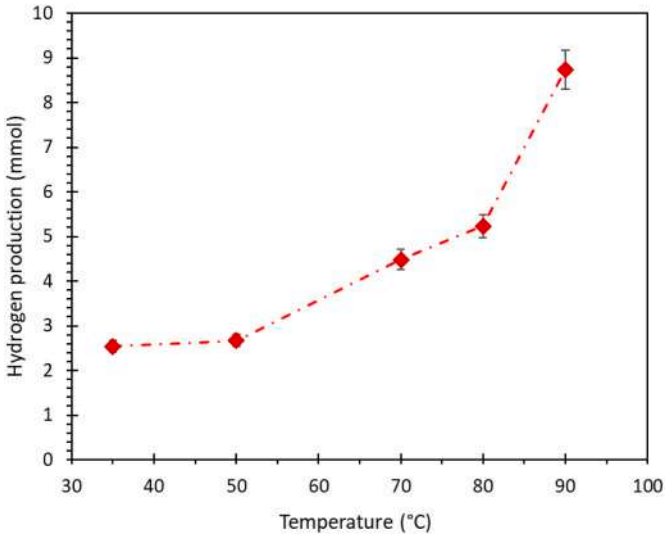

Fig. 12. Hydrogen amount produced with varying the temperature of the system between 35 and 90°C. Experimental conditions: C_{cat} = 0.8 g L^{-1}; [Glycerol] = 0.05 M; V = 0.25 L; pH ~ 5.5; UV + Visible light radiation.

represents a promising candidate for hydrogen production using solar energy, as it enhances the utilization of the solar spectrum. This result can be attributed to the improved visible light absorbance of the (93% wt.)TiO_2/(2%wt.)Cu_2O/(5%wt.)$LaFeO_3$ material with respect to bare TiO_2, as evidenced by the UV–visible absorption spectra shown in Fig. 5 (a).

3.3.5. Photocatalyst reusability

Finally, the possibility of reuse the selected photocatalytic material in 5 successive runs were evaluated. The results are presented in Fig. S8, where hydrogen amount produced under during different photocatalytic cycles in the presence of (93%wt.)TiO_2/(2%wt.)Cu_2O/(5%wt.)$LaFeO_3$ is shown. The experimental results showed a slight decrease of hydrogen production after each cycle, probably due to some modifications occurring in the photocatalyst ascribed to the presence of Cu_2O as reported previously [32]. The spent photocatalyst for (86.14%wt.) TiO_2/(10%wt.)CuO/(3.86%wt.)$LaFeO_3$ and (93%wt.)TiO_2/(2%wt.) Cu_2O/(5%wt.)$LaFeO_3$ were charachterized to investigate any chemical or structural changes. Accordingly, the XRD (Fig. S4) measured before and after the photocatalytic reaction showed no significant changes in peak positions on intensity, confirming the structural stability of the

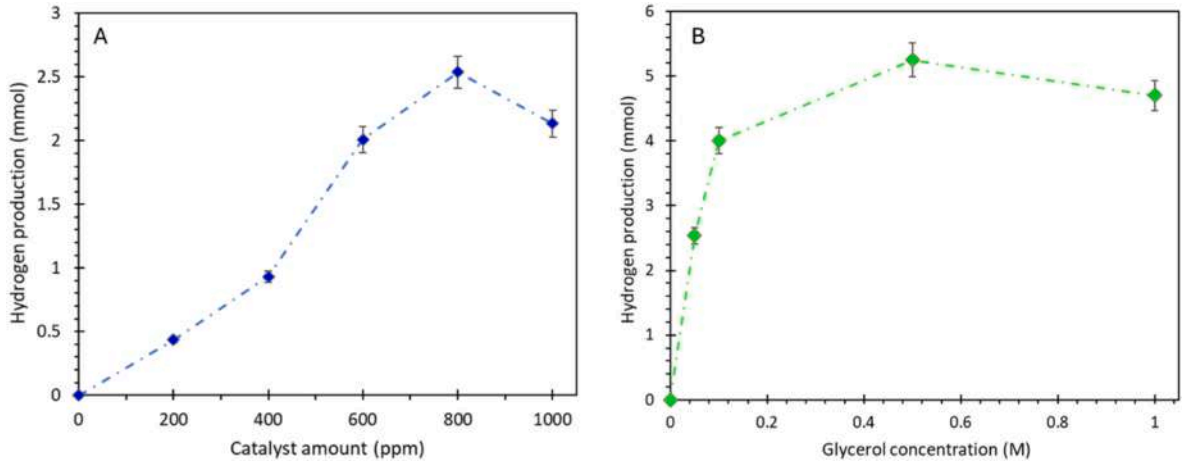

Fig. 11. Hydrogen produced amount after 3 h of irradiation at varying (A) catalyst amount (0 ÷ 1 g L^{-1}) and (B) sacrificial agent concentration (0 ÷ 1 M). Experimental conditions: V = 0.25 L; pH ~ 5.5; T = 35°C; UV + Visible light radiation; (A) [Glycerol] = 0.05 M; (B) C_{cat} = 0.8 g L^{-1}.

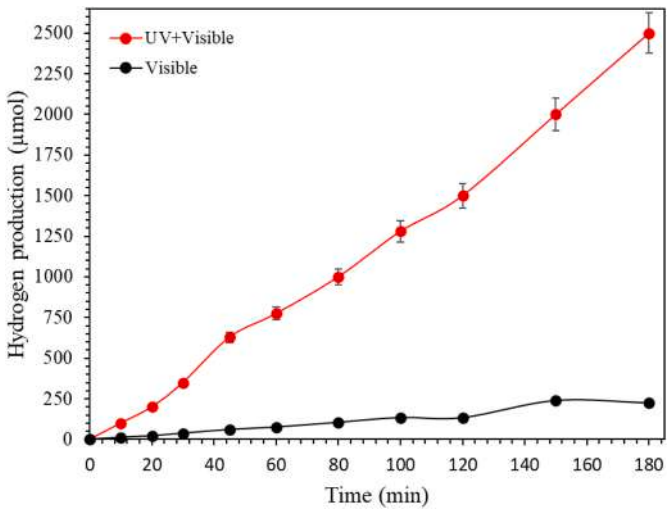

Fig. 13. Hydrogen amount produced under UV + Visible light irradiation (Red line) and Visible light irradiation (Black line). Experimental conditions: C_{cat} = 0.8 g L^{-1}; [Glycerol] = 0.05 M; V = 0.25 L; pH ~ 5.5; T = 35°C. (For interpretation of the references to colour in this figure legend, the reader is referred to the Web version of this article.)

photocatalysts. Post-reaction XPS analysis (Fig. S5 and S6) revealed the most significant changes in the Cu 2p and Ti 2p spectra of both composite samples. The Cu 2p spectra show an increased Cu^{+} contribution after the reaction, confirming the reduction of Cu^{2+} to Cu^{+} via interfacial electron transfer from the TiO_2 conduction band, with this effect being more pronounced in (86.14%wt.)TiO_2/(10%wt.)CuO/(3.86%wt.)$LaFeO_3$ due to its higher CuO loading. Consistently, an increase in the Ti^{3+} shoulder at ~457 eV was observed in both post-reaction Ti 2p spectra, attributed to photogenerated electron trapping within the TiO_2 lattice.

4. Reaction mechanism

Fig. 14 shows a proposed mechanism involving photocatalytic hydrogen generation and glycerol oxidation over (93%wt.)TiO_2/(2%wt.)Cu_2O/(5%wt.)$LaFeO_3$ catalysts. Firstly, UV irradiation generates hole-electron pairs on each semiconductor. These charge carriers can rapidly recombine producing light and heat, or, alternatively, charge carriers can be scavenged. The presence of adsorbed glycerol significantly inhibits charge carrier recombination, as photogenerated holes react with the organic strongly adsorbed on the (93%wt.)TiO_2/(2%wt.)Cu_2O/(5%wt.)$LaFeO_3$ photocatalyst surface, releasing protons into the

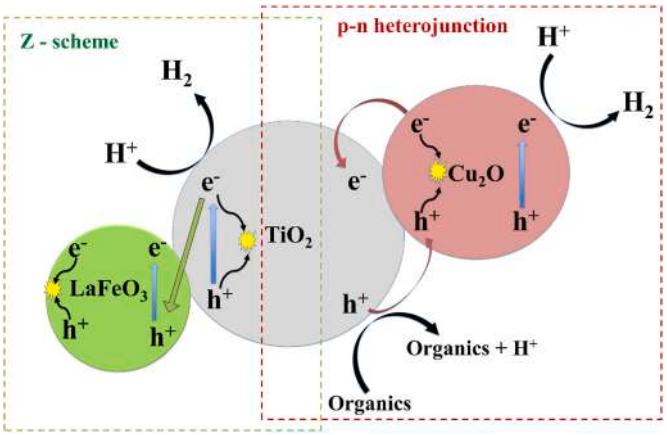

Fig. 14. Photocatalytic reaction mechanism for H_2 generation and glycerol oxidation over (93%wt.)TiO_2/(2%wt.)Cu_2O/(5%wt.)$LaFeO_3$ photocatalyst.

aqueous suspension. The presence of Cu_2O leads the formation of p-n heterojuncion [14,32], while a direct Z-scheme [75] can be proposed due to the presence of $LaFeO_3$ [26]. These proposed charge transfer pathways are supported by the available experimental evidence: the reduced PL emission intensity of the composite samples relative to bare TiO_2 could suggest suppressed electron-hole recombination consistent with heterojunction charge transfer, and the XPS Cu 2p data confirming the reduction of Cu^{2+} to Cu^{+} in the composite is consistent with interfacial electron transfer from the TiO_2 conduction band [51–53]. These phenomena reduce the electron-holes recombination rate and improve the photocatalytic activity. Furthermore, the enhanced photocatalytic H_2 evolution activity of the ternary composites relative to binary and single-component systems provides indirect functional evidence of effective charge separation within the heterojunction. As a consequence, the protons are reduced to molecular hydrogen on both titanium dioxide and cuprous oxide, while the unsuitable band gap position of $LaFeO_3$ avoids the formation of hydrogen on this semiconductor [26].

5. Conclusions

The present study demonstrates that compositional optimization plays a crucial role in maximizing the synergistic efficiency of Cu-based $LaFeO_3$/TiO_2 ternary photocatalysts for hydrogen production via photoreforming. The integration of Cu oxides with $LaFeO_3$ and TiO_2 significantly enhances photocatalytic activity by promoting charge separation and extending light absorption. A clear distinction between the two copper-based systems emerges from the results. The CuO-based ternary composite exhibits the highest initial photocatalytic activity, reaching up to 828 μmol of H_2 after 3 h under UV–visible irradiation, highlighting its strong intrinsic reactivity. However, this system suffers from poor reproducibility and reduced stability after ball milling, which limits its practical applicability and scalability. In contrast, the Cu_2O-based $LaFeO_3$/TiO_2 composite, although less active in terms of initial hydrogen production, demonstrates superior stability, reproducibility, and improved performance after ball milling, with hydrogen production increasing from 338 to 440 μmol in 3 h (approximately 6-fold higher than bare TiO_2). These features make the Cu_2O-based system more suitable for practical applications where robustness and process reliability are essential.

Under optimized operating conditions (C_{cat} = 0.8 g L^{-1}, [Glycerol] = 0.05 M, T = 90°C), hydrogen production reaches values up to ~9000 μmol, corresponding to an enhancement of approximately 20-fold compared to baseline conditions. Importantly, these results are achieved while maintaining the advantages of a simple, scalable, and environmentally friendly preparation method based on dry ball milling.

Overall, while CuO-based systems are promising for applications requiring maximum short-term activity, Cu_2O-based ternary composites offer a more balanced combination of performance, stability, and scalability, making them more suitable for long-term and large-scale hydrogen production.

Future work should focus on long-term stability assessment, deeper mechanistic investigations, and validation under real solar irradiation conditions to further advance the practical implementation of these materials in sustainable hydrogen production technologies.

CRediT authorship contribution statement

Marica Muscetta: Conceptualization, Data curation, Formal analysis, Investigation, Methodology, Writing – original draft, Writing – review & editing. **Isabella Natali Sora:** Conceptualization, Investigation, Methodology, Writing – original draft. **Renato Pelosato:** Conceptualization, Methodology, Writing – original draft. **Adetunji Alabi:** Data curation, Investigation, Methodology, Writing – original draft. **Israa Othman:** Data curation, Investigation, Methodology, Writing – original draft. **Mohammad Abu Haija:** Data curation, Investigation, Methodology, Writing – original draft. **Giovanni Palmisano:**

Conceptualization, Supervision, Writing – original draft. **Roberto Andreozzi:** Supervision, Writing – original draft. **Laura Clarizia:** Conceptualization, Data curation, Investigation, Writing – original draft, Writing – review & editing.

Declaration of competing interest

The authors declare that they have no known competing financial interests or personal relationships that could have appeared to influence the work reported in this paper.

Acknowledgement

M.M. acknowledges the project "NEST – Network 4 Energy Sustainable Transition PE2" PE0000021 CUP: E63C22002160007, for the financial support. The authors acknowledge Nurlan Akhmetov for ICP-OES characterizations, and Research & Innovation Center for Graphene and 2D Materials (RIC2D), Khalifa University, for FTIR access. The authors gratefully acknowledge the Core Labs at Khalifa University for providing access to advanced characterization facilities. Support from the Research and Innovation Center on CO_2 and Hydrogen (RICH) at Khalifa University is also gratefully acknowledged.

Appendix A. Supplementary data

Supplementary data to this article can be found online at https://doi.org/10.1016/j.ijhydene.2026.156682.

References

[1] Akpasi SO, Smarte Anekwe IM, Tetteh EK, Amune UO, Mustapha SI, Kiambi SL. Hydrogen as a clean energy carrier: advancements, challenges, and its role in a sustainable energy future. Clean Energy 2025;9:52–88. https://doi.org/10.1093/CE/ZKAE112.

[2] Rehan MA, Li G, Liang H, Ali M. Recent advances in hybrid photocatalysts for efficient solar photocatalytic hydrogen production. Int J Hydrogen Energy 2025;97:920–49. https://doi.org/10.1016/J.IJHYDENE.2024.11.420.

[3] Tak SS, Shetye O, Muley O, Jaiswal H, Malik SN. Emerging technologies for hydrogen production from wastewater. Int J Hydrogen Energy 2022;47:37282–301. https://doi.org/10.1016/j.ijhydene.2022.06.225.

[4] Yang S, Wang H, Yu H, Zhang S, Fang Y, Zhang S, Peng F. A facile fabrication of hierarchical Ag nanoparticles-decorated N-TiO2 with enhanced photocatalytic hydrogen production under solar light. Int J Hydrogen Energy 2016;41:3446–55. https://doi.org/10.1016/J.IJHYDENE.2015.12.190.

[5] Leung DYC, Fu X, Wang C, Ni M, Leung MKH, Wang X, Fu X. Hydrogen production over titania-based photocatalysts. ChemSusChem 2010;3:681–94. https://doi.org/10.1002/cssc.201000014.

[6] Wang G, Lv S, Shen Y, Li W, Lin L, Li Z. Advancements in heterojunction, cocatalyst, defect and morphology engineering of semiconductor oxide photocatalysts. J Materiomics 2024;10:315–38. https://doi.org/10.1016/J.JMAT.2023.05.014.

[7] Chiarello GL, Dozzi MV, Selli E. TiO2-based materials for photocatalytic hydrogen production. J Energy Chem 2017;26:250–8. https://doi.org/10.1016/J.JECHEM.2017.02.005.

[8] Sudrajat H, Sudrajat H, Sudrajat H, Nobatova M. Heterojunction photocatalysts: where are they headed? RSC Applied Interfaces 2025;2:599–619. https://doi.org/10.1039/D5LF00037H.

[9] Greco R, Botella R, Fernández-Catalá J. Cu-Based Z-Schemes family photocatalysts for solar H2 production. Hydro 2023;4:620–43. https://doi.org/10.3390/HYDROGEN4030040. 4 (2023) 620–643.

[10] Kurenkova AY, Yakovleva AY, Saraev AA, Gerasimov EY, Kozlova EA, Kaichev VV. Copper-modified titania-based photocatalysts for the efficient hydrogen production under UV and visible light from aqueous solutions of glycerol. Nanomaterials 2022;12:3106. https://doi.org/10.3390/NANO12183106/S1.

[11] Hu Q, Huang J, Li G, Jiang Y, Lan H, Guo W, Cao Y. Origin of the improved photocatalytic activity of Cu incorporated TiO 2 for hydrogen generation from water. Appl Surf Sci 2016;382:170–7. https://doi.org/10.1016/j.apsusc.2016.04.126.

[12] Li Y, Wang B, Liu S, Duan X, Hu Z. Synthesis and characterization of Cu 2 O/TiO 2 photocatalysts for H 2 evolution from aqueous solution with different scavengers. Appl Surf Sci 2015;324:736–44. https://doi.org/10.1016/J.APSUSC.2014.11.027.

[13] Muscetta M, Andreozzi R, Clarizia L, Di Somma I, Marotta R. Hydrogen production through photoreforming processes over Cu2O/TiO2 composite materials: a mini-review. Int J Hydrogen Energy 2020;45:28531–52. https://doi.org/10.1016/j.ijhydene.2020.07.225.

[14] Muscetta M, Clarizia L, Race M, Andreozzi R, Marotta R, Di Somma I. Visible—light driven systems: effect of the parameters affecting hydrogen production through photoreforming of organics in presence of Cu2O/TiO2 nanocomposite photocatalyst. Appl Sci (Switzerland) 2023;13. https://doi.org/10.3390/app13042337.

[15] Khan AA, Partho AT, Arnab MH, Khyam MA, Kumar N, Tahir M. Recent advances in Lanthanum-based photocatalysts with engineering aspects for photocatalytic hydrogen production: a critical review. Mater Sci Semicond Process 2024;184:108809. https://doi.org/10.1016/J.MSSP.2024.108809.

[16] Theingi M, Tun KT, Aung NN. Preparation, characterization and optical property of LaFeO3 nanoparticles via sol-Gel combustion method. Sci Med J 2019;1:151–7. https://doi.org/10.28991/SCIMEDJ-2019-0103-5.

[17] Peng K, Fu L, Yang H, Ouyang J. Perovskite LaFeO3/montmorillonite nanocomposites: synthesis, interface characteristics and enhanced photocatalytic activity. Sci Rep 2016;6:1–10. https://doi.org/10.1038/SREP19723;SUBJMETA=298,301,638,639,923;KWRD=MATERIALS+CHEMISTRY,SOFT+MATERIALS.

[18] Humayun M, Ullah H, Usman M, Habibi-Yangjeh A, Tahir AA, Wang C, Luo W. Perovskite-type lanthanum ferrite based photocatalysts: preparation, properties, and applications. J Energy Chem 2022;66:314–38. https://doi.org/10.1016/J.JECHEM.2021.08.023.

[19] Raji RK, Ramachandran T, Muralidharan M, Suriakarthick R, Dhilip M, Raja A, Aravinth K, Karthikeyan S, Ramasamy P, Kurapati V, Hamed F, Mourad AHI. Dual-phase formation in LaFeO3 upon doping of rare-earth Dy3+: struct–opto–dielectric–magnetic characteristics. J Mater Sci Mater Electron 2022;33:10626–44. https://doi.org/10.1007/S10854-022-08047-6/TABLES/4.

[20] Sora IN, Fontana F, Passalacqua R, Ampelli C, Perathoner S, Centi G, Parrino F, Palmisano L. Photoelectrochemical properties of doped lanthanum orthoferrites. Electrochim Acta 2013;109:710–5. https://doi.org/10.1016/J.ELECTACTA.2013.07.132.

[21] Sánchez-Jiménez AF, Blázquez PE, Li W, Wen Q, Li F, Manchón-Gordón AF, Sánchez-Jiménez PE, Blázquez JS, Perejón A, Pérez-Maqueda LA. Structural, vibrational, and magnetic characterization of orthoferrite LaFeO3 ceramic prepared by reaction flash sintering. Materials 2023;16:1019. https://doi.org/10.3390/MA16031019. 2023, Vol. 16, Page 1019.

[22] Kotnana G, Hong S. Recent progress on rare Earth orthoferrites for gas-sensing applications. Chemosensors 2025;13:156. https://doi.org/10.3390/CHEMOSENSORS13050156. 2025, Vol. 13, Page 156.

[23] Yu J, Wang C, Yuan Q, Yu X, Wang D, Chen Y. Ag-Modified porous perovskite-type LaFeO3 for efficient ethanol detection. Nanomaterials 2022;12:1768. https://doi.org/10.3390/NANO12101768/S1.

[24] Hou L, Wang Y, Zhou F, Liu S, Fu L, Wang L, Zhang C, Xue W. A visible-light-enhanced heterogeneous photo degradation of tetracycline by a Nano-LaFeO3 catalyst with the assistance of persulfate. Nanomaterials 2023;13:1388. https://doi.org/10.3390/NANO13081388.

[25] Jiang Y, Lv Q, Xu F, Sun X, Ding Y. Synthesis of TiO2/LaFeO3 composites for the photoelectrochemical hydrogen evolution. J Mater Sci 2021;56:15188–204. https://doi.org/10.1007/S10853-021-06188-3.

[26] Natali Sora I, Bertolotti B, Pelosato R, Lucotti A, Tommasini M, Muscetta M. TiO2/LaFeO3 composites for the efficient degradation of benzoic acid and hydrogen production. Molecules 2025;30:1526. https://doi.org/10.3390/MOLECULES30071526/S1.

[27] Chen S, Zhao W, Liu W, Zhang S. Preparation, characterization and activity evaluation of p–n junction photocatalyst p-ZnO/n-TiO2. Appl Surf Sci 2008;255:2478–84. https://doi.org/10.1016/J.APSUSC.2008.07.115.

[28] Han C, Shao Q, Lei J, Zhu Y, Ge S. Preparation of NiO/TiO2 p-n heterojunction composites and its photocathodic protection properties for 304 stainless steel under simulated solar light. J Alloys Compd 2017;703:530–7. https://doi.org/10.1016/J.JALLCOM.2017.01.349.

[29] Shifu C, Sujuan Z, Wei L, Wei Z. Preparation and activity evaluation of p–n junction photocatalyst NiO/TiO2. J Hazard Mater 2008;155:320–6. https://doi.org/10.1016/J.JHAZMAT.2007.11.063.

[30] Ma R, Williams G, Muscetta M, Vernuccio S. Enhanced photocatalytic hydrogen evolution via ball-milled PtO2/TiO2 heterojunction photocatalyst: an alternative approach for efficient energy production. Chem Eng J 2025;507. https://doi.org/10.1016/j.cej.2025.160228.

[31] Bolognino I, Pelosato R, Marcì G, Natali Sora I. Comparison of ten metal-doped LaFeO3 samples on photocatalytic degradation of antibiotics in water under visible light: role of surface area and aqueous phosphate ions. Molecules 2023;28:3807. https://doi.org/10.3390/molecules28093807.

[32] Muscetta M, Al Jitan S, Palmisano G, Andreozzi R, Marotta R, Cimino S, Di Somma I. Visible light – driven photocatalytic hydrogen production using Cu2O/TiO2 composites prepared by facile mechanochemical synthesis. J Environ Chem Eng 2022;10:107735. https://doi.org/10.1016/j.jece.2022.107735.

[33] Russo D, Muscetta M, Clarizia L, Di Somma I, Garlisi C, Marotta R, Palmisano G, Andreozzi R. Photoactivated Fe(III)/Fe(II)/WO3–Pd fuel cell for electricity generation using synthetic and real effluents under visible light. Renew Energy 2020;147:1070–81. https://doi.org/10.1016/j.renene.2019.09.080.

[34] Chang Y, Xu J, Zhang Y, Ma S, Xin L, Zhu L, Xu C. Optical properties and photocatalytic performances of Pd modified ZnO samples. J Phys Chem C 2009;113:18761–7. https://doi.org/10.1021/jp9050808.

[35] Holzwarth U, Gibson N. The Scherrer equation versus the "Debye-Scherrer equation,". Nat Nanotechnol 2011;6(9 6). https://doi.org/10.1038/nnano.2011.145. 534–534.

[36] Horti NC, Kamatagi MD, Patil NR, Nataraj SK, Sannaikar MS, Inamdar SR. Synthesis and photoluminescence properties of titanium oxide (TiO2) nanoparticles: effect of calcination temperature. Optik 2019;194:163070. https://doi.org/10.1016/J.IJLEO.2019.163070.

[37] Vijayaraghavan T, Sivasubramanian R, Hussain S, Ashok A. A Facile synthesis of LaFeO3-Based perovskites and their application towards sensing of neurotransmitters. ChemistrySelect 2017;2:5570–7. https://doi.org/10.1002/SLCT.201700723.
[38] Sedumathavan K, Sivakumar N, Alsulmi A, Kumar KY, Settu K. A comprehensive exploration of pure and Zn doped LaFeO3 nanoparticles synthesized by solid state mechanism for charge storage devices. J Mater Sci Mater Electron 2024;35:1–15. https://doi.org/10.1007/S10854-024-13483-7/TABLES/5.
[39] Pagare PK, Torane AP. Band gap varied cuprous oxide (Cu2O) thin films as a tool for glucose sensing. Microchim Acta 2016;183:2983–9. https://doi.org/10.1007/S00604-016-1949-6/FIGURES/5.
[40] Thirumalairajan S, Girija K, Hebalkar NY, Mangalaraj D, Viswanathan C, Ponpandian N. Shape evolution of perovskite LaFeO3 nanostructures: a systematic investigation of growth mechanism, properties and morphology dependent photocatalytic activities. RSC Adv 2013;3:7549–61. https://doi.org/10.1039/C3RA00006K.
[41] Kaur H, Goyal V, Singh J, Kumar S, Rawat M. Biomolecules encapsulated TiO2 nano-cubes using Tinospora cordifolia for photodegradation of a textile dye. Micro & Nano Lett 2019;14:1229–32. https://doi.org/10.1049/MNL.2019.0340.
[42] Khalifa M, El Sayed AM, Kassem SM, Tarek E. Synthesis, structural, optical, and thermal properties of LaFeO3/Poly(methyl methacrylate)/Poly(vinyl acetate) nanocomposites for radiation shielding. Sci Rep 2024;14:1–17. https://doi.org/10.1038/S41598-024-54207-5;SUBJMETA=301,624,639,766,925;KWRD=MATERIALS+SCIENCE,NANOSCIENCE+AND+TECHNOLOGY,OPTICS+AND+PHOTONICS,PHYSICS.
[43] Su D, Xie X, Dou S, Wang G. CuO single crystal with exposed {001} facets - A highly efficient material for gas sensing and Li-ion battery applications. Sci Rep 2014;4(1 4):1–9. https://doi.org/10.1038/srep05753. 2014.
[44] Hamdan S, Wigglesworth MJ, Muscetta M, Ma R, Helal MI, Martsinovich N, Palmisano G, Vernuccio S. Unravelling the photoactivity of metal-loaded TiO2 for hydrogen production: insights from a combined experimental and computational analysis. Int J Hydrogen Energy 2025;118:394–406. https://doi.org/10.1016/J.IJHYDENE.2025.03.184.
[45] Ashok CH, Venkateswara Rao K. Microwave-assisted synthesis of CuO/TiO2 nanocomposite for humidity sensor application. J Mater Sci Mater Electron 2016;27:8816–25. https://doi.org/10.1007/S10854-016-4907-5/METRICS.
[46] Hosseini SM, Asadpour S, Ghasemi M, Shirani M. Efficient photocatalytic activity of ZnO/GO/CuO nanocomposite with solar light for reduction of hexavalent chromium. Sci Rep 2025;15. https://doi.org/10.1038/S41598-025-05790-8.
[47] Sahu DP, Jammalamadaka SN. Detection of bovine serum albumin using hybrid TiO2 + graphene oxide based Bio – resistive random access memory device. Sci Rep 2019;9:1–10. https://doi.org/10.1038/S41598-019-52522-W;TECHMETA=120,128;SUBJMETA=1005,1007,1052,301,639,918,925;KWRD=ELECTRONIC+DEVICES,ELECTRONIC+PROPERTIES+AND+DEVICES.
[48] Zhu K, Zhu Q, Jiang M, Zhang Y, Shao Z, Geng Z, Wang X, Zeng H, Wu X, Zhang W, Huang K, Feng S. Modulating Ti t2g orbital occupancy in a Cu/TiO2 composite for selective photocatalytic CO2 reduction to CO. Angew Chem Int Ed 2022;61:e202207600. https://doi.org/10.1002/ANIE.202207600;REQUESTEDJOURNAL:JOURNAL:15213773;CTYPE:STRING:JOURNAL.
[49] Yuan W, Wu Y, Fang C, Wang X, Huang X, Li C. Engineering nanowire array structure of copper Oxide/Cuprous oxide for enhanced oxygen evolution reaction. J Electrochem Soc 2020;167:022508. https://doi.org/10.1149/1945-7111/AB6978.
[50] Hamad H, Elsenety MM, Sadik W, El-Demerdash AG, Nashed A, Mostafa A, Elyamny S. The superior photocatalytic performance and DFT insights of S-scheme CuO@TiO2 heterojunction composites for simultaneous degradation of organics. Sci Rep 2022;12(1 12):1–20. https://doi.org/10.1038/s41598-022-05981-7. 2022.
[51] Díaz L, Rodríguez VD, González-Rodríguez M, Rodríguez-Castellón E, Algarra M, Núñez P, Moretti E. M/TiO2 (M = Fe, Co, Ni, Cu, Zn) catalysts for photocatalytic hydrogen production under UV and visible light irradiation. Inorg Chem Front 2021;8:3491–500. https://doi.org/10.1039/D0QI01311K.
[52] Huang X, Zhang M, Sun R, Long G, Liu Y, Zhao W. Enhanced hydrogen evolution from CuOx-C/TiO2 with multiple electron transport pathways. PLoS One 2019;14. https://doi.org/10.1371/JOURNAL.PONE.0215339.
[53] Montoya AT, Gillan EG. Enhanced photocatalytic hydrogen evolution from transition-metal surface-modified TiO2. ACS Omega 2018;3:2947–55. https://doi.org/10.1021/ACSOMEGA.7B02021.
[54] Bhattacharya S, Das R, Chowdhury S, Supin KK, Vasundhara M, Sahu JR, Bhunia T, Gayen A, Lebedev OI, Seikh MM. Entanglement of cation ordering and manipulation of the magnetic properties through a temperature-controlled topotactic interface reaction in nanocomposite perovskite oxides. Mater Adv 2024;5:3863–80. https://doi.org/10.1039/D3MA00891F.
[55] Hara M, Kondo T, Komoda M, Ikeda S, Kondo JN, Domen K, Hara M, Shinohara K, Tanaka A. Cu2O as a photocatalyst for overall water splitting under visible light irradiation. Chem Commun 1998:357–8. https://doi.org/10.1039/a707440i.
[56] Tachibana Y, Muramoto R, Matsumoto H, Kuwabata S. Photoelectrochemistry of p-type Cu2O semiconductor electrode in ionic liquid. Res Chem Intermed 2006;32:575–83. https://doi.org/10.1163/156856706777973637.
[57] Jeyalakshmi V, Mahalakshmy R, Krishnamurthy KR, Viswanathan B. Photocatalytic reduction of carbon dioxide by water: a step towards sustainable fuels and chemicals. Mater Sci Forum 2013;734:1–62. https://dx.doi.org/10.4028/www.scientific.net/MSF.734.1.
[58] Toe CY, Scott J, Amal R, Ng YH. Recent advances in suppressing the photocorrosion of cuprous oxide for photocatalytic and photoelectrochemical energy conversion. J Photochem Photobiol C Photochem Rev 2019;40:191–211. https://doi.org/10.1016/j.jphotochemrev.2018.10.001.
[59] Toe CY, Zheng Z, Wu H, Scott J, Amal R, Ng YH. Photocorrosion of cuprous oxide in hydrogen production: rationalising self-oxidation or self-reduction. Angew Chem 2018;130:13801–5. https://doi.org/10.1002/ange.201807647.
[60] Ruiz-Aguirre A, Villachica-Llamosas JG, Polo-López MI, Cabrera-Reina A, Colón G, Peral J, Malato S. Assessment of pilot-plant scale solar photocatalytic hydrogen generation with multiple approaches: valorization, water decontamination and disinfection. Energy 2022;260. https://doi.org/10.1016/j.energy.2022.125199.
[61] Chandran SV, Narayanan BN. Copper oxide incorporated ball-mill produced less-defective graphene for hybrid supercapacitors. Diam Relat Mater 2024;143:110842. https://doi.org/10.1016/j.diamond.2024.110842.
[62] Bellardita M, García-López EI, Marcì G, Nasillo G, Palmisano L. Photocatalytic solar light H2 production by aqueous glucose reforming. Eur J Inorg Chem 2018;2018:4522–32. https://doi.org/10.1002/ejic.201800663.
[63] Wang X, Dong H, Hu Z, Qi Z, Li L. Fabrication of a Cu2O/Au/TiO2composite film for efficient photocatalytic hydrogen production from aqueous solution of methanol and glucose. Mater Sci Eng B Solid State Mater Adv Technol 2017;219:10–9. https://doi.org/10.1016/j.mseb.2017.02.011.
[64] Kou J, Lu C, Wang J, Chen Y, Xu Z, Varma RS. Selectivity enhancement in heterogeneous photocatalytic transformations. Chem Rev 2017;117:1445–514. https://doi.org/10.1021/ACS.CHEMREV.6B00396/ASSET/IMAGES/MEDIUM/CR-2016-003966_0044.GIF.
[65] Rueda-Navarro CM, Ferrer B, Baldoví HG, Navalón S. Photocatalytic hydrogen production from glycerol aqueous solutions as sustainable feedstocks using Zr-Based UiO-66 materials under simulated sunlight irradiation. Nanomaterials 2022;12:3808. https://doi.org/10.3390/NANO12213808/S1.
[66] Guo M, Zhang M, Liu R, Zhang X, Li G. State-of-the-Art advancements in photocatalytic hydrogenation: reaction mechanism and recent progress in metal-organic framework (MOF)-Based catalysts. Adv Sci 2022;9:2103361. https://doi.org/10.1002/ADVS.202103361;SUBPAGE:STRING:FULL.
[67] Clarizia L, Vitiello G, Luciani G, Di Somma I, Andreozzi R, Marotta R. In situ photodeposited nanoCu on TiO2 as a catalyst for hydrogen production under UV/visible radiation. Appl Catal Gen 2016;518:142–9. https://doi.org/10.1016/j.apcata.2015.07.044.
[68] Panagiotopoulou P, Karamerou EE, Kondarides DI. Kinetics and mechanism of glycerol photo-oxidation and photo-reforming reactions in aqueous TiO2 and Pt/TiO2 suspensions. Catal Today 2013;209:91–8. https://doi.org/10.1016/J.CATTOD.2012.09.029.
[69] Ghosh S, Küçükkeçeci H, Paitandi RP, Weigelt V, Dippold V, Seki S, Thomas A. Low band gap semiconducting covalent organic framework films with enhanced photocatalytic hydrogen evolution. J Mater Chem A 2024;12:247–55. https://doi.org/10.1039/D3TA04552H.
[70] Maurino V, Bedini A, Minella M, Rubertelli F, Pelizzetti E, Minero C. Glycerol transformation through photocatalysis: a possible route to value added chemicals. J Adv Oxid Technol 2008;11. http://www.environmentalchemistry.unito.it.
[71] Ciriminna R, Della Pina C, Rossi M, Pagliaro M. Understanding the glycerol market. Eur J Lipid Sci Technol 2014;116:1432–9. https://doi.org/10.1002/ejlt.201400229.
[72] Gao M, Zhang T, Ho GW. Advances of photothermal chemistry in photocatalysis, thermocatalysis, and synergetic photothermocatalysis for solar-to-fuel generation. Nano Res 2022. https://doi.org/10.1007/s12274-022-4795-3.
[73] Chen YW, Hsu YH. Effects of reaction temperature on the photocatalytic activity of TiO2 with Pd and Cu cocatalysts. Catalysts 2021;11:966. https://doi.org/10.3390/CATAL11080966. 11 (2021) 966.
[74] Huaxu L, Fuqiang W, Ziming C, Shengpeng H, Bing X, Xiangtao G, bo L, Jianyu T, Xiangzheng L, Ruiyang C, Wen L, Linhua L. Analyzing the effects of reaction temperature on photo-thermo chemical synergetic catalytic water splitting under full-spectrum solar irradiation: an experimental and thermodynamic investigation. Int J Hydrogen Energy 2017;42:12133–42. https://doi.org/10.1016/j.ijhydene.2017.03.194.
[75] Yue C, Sun N, Qiu Y, Zhu L, Du Z, Liu F. A direct Z-s che me 0D α-Fe2O3/TiO2 heterojunction for enhanced photo-Fenton activity with low H2O2 consumption. Chin Chem Lett 2024;35:109698. https://doi.org/10.1016/J.CCLET.2024.109698.